Thermoelastic and Ablative Laser Generation of Ultrasonic Waveforms in Graphite/Polymer Composite Materials

James N. Caron, Yuqiao Yang, and James B. Mehl
Department of Physics & Astronomy, University of Delaware, Newark, DE 19716-2570
Karl V. Steiner
Center for Composite Materials, University of Delaware, Newark DE 19716-3144

For submittal to *Journal of Applied Physics* — 21 May 1998

Abstract

A laser-based ultrasonic system was used to study thermoelastic and ablative ultrasonic laser generation mechanisms in graphite/polymer composite structures. Ultrasonic waveforms were generated in 16-layer quasi-isotropic AS-4/PEEK composite and 8-layer thick AS-4/PEKK $[0/90]_{2S}$ composite panels. Waveforms generated on one side of the samples were observed on the opposite side using a confocal Fabry-Perot (CFP) based detection system. The waveforms, as functions of the generation-laser power density, show that there are two distinct generation mechanisms. Below a well-defined threshold power density, the observed signals were proportional to the power density and are assumed to be generated thermoelastically. Above the threshold the observed waveforms are a superposition of a thermoelastic (TE) and ablatic (AB) waveforms. The relative amplitudes of the TE and AB components were determined as a function of power density by fitting a theoretical model to the data. The ablation threshold was independently observed through photodetection of the light radiated by the ablation plume. Further experimentation partially characterized the directivity of the generation mechanisms for the graphite/PEEK composite panel.

Introduction

When a laser pulse strikes an opaque material, part of the pulse is reflected and part is absorbed. The absorbed light energy is converted to thermal energy, causing a local thermoelastic expansion of material near the impact point. The rapid expansion creates an thermoelastic (TE) ultrasonic pulse which propagates through the material.[1, 2] Purely thermoelastic generation is limited at higher intensities by the onset of surface melting and vaporization. The laser power density at the point of vaporization is referred to as the ablation threshold.

When the ablation threshold is exceeded, the laser pulse vaporizes surface material. A high-temperature plasma, caused by the rapid heating and ionization of the material, is formed just above the sample. The electromagnetic energy is converted into electronic, thermal, chemical and mechanical energy at the solid surface. The vaporized material may consist of neutral atoms and molecules, posi-

tive and negative ions, clusters, electrons, and photons [3]. A review article by Srinivasan [4] includes excellent photographs of ablation of pure polymers.

These processes have been shown to create an ultrasonic wave, the ablatic (AB) waveform, in the host material in addition to those generated thermoelastically. Although there is a significant amount of ablative generation studies,[5, 6, 7, 8] few have demonstrated the superposition of the two waveforms. An exception is the work of Dyer *et al.* [9], who used wide-band polyvinylidenefluoride film piezoelectric transducers to detect combined thermoelastic/ablatic waveforms in 12 μm thick polymethylmethacrylate films.

In this work, A laser-based system was used to study thermoelastic and ablative ultrasonic generation mechanisms in graphite/polymer composite materials. Ultrasonic waveforms were generated in 16 layer (2.9 mm thick) quasi-isotropic AS-4/PEEK composite and 8 layer (1.5 mm thick) AS-4/PEKK $[0/90]_{2S}$ composite. The superposition of thermoelastic and ablatic waveforms occurred when the laser power density exceeded the ablation threshold. Detection was accomplished by using a confocal Fabry-Perot (CFP) interferometric system [10]. The ultrasonic signal was derived from light reflected from the CFP interferometer to take advantage of the improved frequency response [11, 12]. Photodetection of light produced by the ablation plume provided independent confirmation of the ablation threshold. The directivity characteristics of the laser-generated TE and resolved AB waveforms were studied for the AS-4/PEEK composite panel.

Measurement of the Ablation Threshold

Before a quantitative study of the waveform generation mechanisms is discussed, the method used to identify the ablation threshold power density I_{ab}, will be described. The threshold I_{ab} is defined as the lowest power density level at which laser ablation is detected. The method uses a photodetector to capture the light produced during laser ablation. The amplitudes of the resulting signals will be used to compare I_{ab} measured in this fashion to the power density at which an ablatic wave is first detected.

A photodetector was placed near the sample, as shown in Figure 1. A pulsed Nd:YAG laser, producing an infrared pulse with approximately 5 ns width, was directed towards the AS-4/PEEK composite panel. The detector was fitted with a filter to block most of the initial infrared laser light and pass most of the visible light. The purpose was to capture only the light produced by the ablation plume. With this configuration, the signal amplitude from the ablation detector can be measured concurrently with the detection of the laser-generated waveforms.

Figure 2 shows a series of photodetected plume signals plotted as a function of time and source power density. For power densities below 60 MW/cm^2, the photodetector picked up only a weak trace of the generating beam. Strong signals evolve at higher power densities. The signals have rise times on the order of 120 ns and decay times longer than 1 μs. Figure 2 also shows the maximum amplitudes plotted as a function of laser power density. The results strongly suggest a parabolic dependence of the form

$$P(I) = \begin{cases} a & \text{for I} < \text{I}_{\text{ab}} \\ a + b(I - I_{ab})^p & \text{for I} \geq \text{I}_{\text{ab}}, \end{cases} \quad (1)$$

with power $p = 2$. This equation was fitted to the data. The best fit occurred with the parameters $I_{ab} = (59 \pm 2)$ MW/cm^2, $a = (-0.061 \pm 0.005)$, and $b = (0.46 \pm 0.02)$. This provides strong evidence for a well-defined threshold.

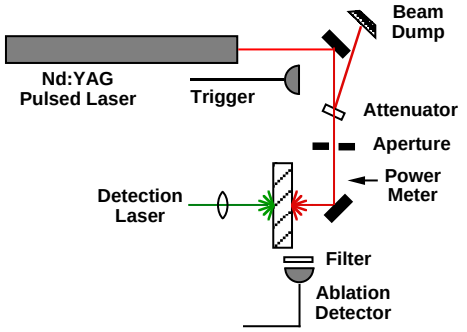

Figure 1: Experimental setup for the study of ablatic waves. A customized photodetector captures light produced by the ablation plume. The aperture and attenuator control the power density range in which the experiments take place.

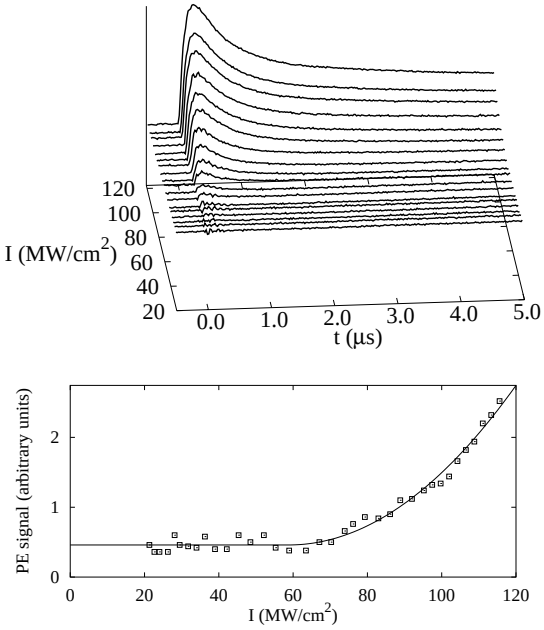

Figure 2: Top: photodetected ablation plume signal vs. time and laser power density. No detectable signal other than electronic noise, is found below the onset of ablation. Bottom: the peak signal from the upper plot as a function of laser power density I. A model with a parabolic dependence above a threshold I_{ab} was fit to the data; the best fit was obtained with threshold power density of $I = 59$ MW/cm^2.

The generating laser power densities reported in this work were determined by measuring the laser power with a power meter and dividing the power by the surface area as measured upon incidence on burn paper. The average power density is then divided by the pulse repetition rate (20 pulses per second) and the pulse width at full-width half-maximum (5 ns), as specified by the manufacturer of the laser [13]. The pulse width has not been verified independently. Using these numbers, a measured power density of 1.0 W/cm^2 translates to a power density of 10 MW/cm^2 per pulse. The typical surface area of the illuminated area is about 0.2 cm^2.

Generation of Ultrasonic Waves across the Ablation Threshold in AS-4/PEEK Composite

The transition from thermoelastic to ablative generation was studied as a function of laser power density. The basic experiment consisted of generating and detecting ultrasonic waveforms as the generating laser power density was varied across the ablation threshold. The generation system is shown in Figure 1. Ultrasonic waves were generated in the AS-4/PEEK composite panel by a pulse of infrared light produced by a Nd:YAG laser. The power density of the pulsed laser was varied by adjusting

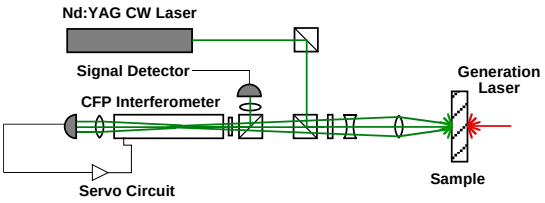

Figure 3: The CFP-based detection system in a reflection configuration. Polarizing beam splitters allow the light reflected from the etalon to be used to derive the ultrasonic signal. Light transmitted through the etalon provides the signal for the servo circuit.

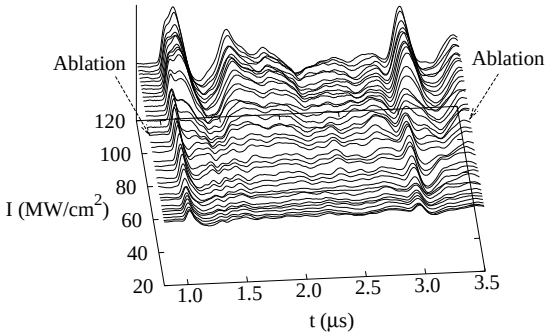

Figure 4: Laser-generated ultrasonic waveforms in 16-layer AS-4/PEEK composite sample with average laser power density I, and detected with the CFP-based system in a through-transmission configuration. The arrows mark the power density at which ablation was first optically observed. A delayed longitudinal pulse and a transverse pulse emerge with increasing power density.

the voltage supplied to the laser flash pump. A variable aperture was inserted to ensure a consistent spot size. An attenuator was inserted to lower the laser energy to a more useful range. The amplitude of the ablation plume signal was also taken at each power density level. Prior to each experiment, a power meter was inserted, at the position shown, to calibrate the laser power density with the digitally displayed flash pump voltage. The detection system is shown in Figure 3. A cw Nd:YAG laser emitted 200 mW of 532 nm light. The vertically polarized light was directed to the sample using polarizing beam splitters (PBS). Surface-reflected light was collected into the CFP interferometer [14] using a telescopic lens system. Light reflected from the CFP etalon was diverted by a PBS to the signal photodetector, providing the signal for the digital oscilloscope. Transmitted light was collected into a second detector providing a reference signal for the servo circuit. The servo circuit, based on a design by White and Emmony [15], was connected to a piezo-electric translator mounted to one of the CFP mirrors. This provides active stabilization of the detection system to counteract normal frequency fluctuations of the laser. The detection-side surface was coated with aluminum paint to enhance the reflectivity, improving the system sensitivity. Starting from moderate thermoelastic power densities (about 21 MW/cm^2), waveforms were captured and averaged over twenty laser shots to reduce the effect of noise in the final data. As the power density was increased, the amount of averaging was reduced to decrease the amount of surface damage done to the composite. Only three waveforms were averaged at the highest power density level.

Figure 4 shows the waveforms plotted as a function of laser power density. The plots represent the surface velocities created by the ultrasonic waves. Looking at the lowest intensity waveform, generated in the low thermoelastic regime, the first peak corresponds to the arrival of the longitudinal wave. Near the detection epicenter, the transverse wave is not

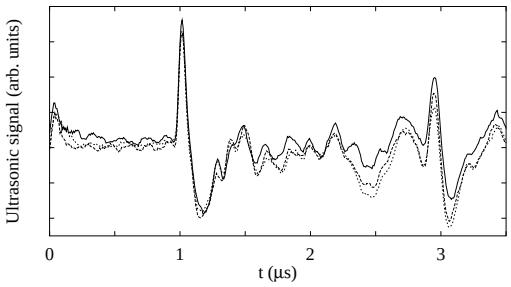

Figure 5: Three waveforms generated at $t = 0$ by power density laser pulses in the thermoelastic regime incident on the AS-4/PEEK composite sample.

discernible. At 3 μs the echo of the longitudinal wave arrives. The shape of the wave does not change as power density is increased in the thermoelastic regime (see also Figure 5). However, starting at about 60 MW/cm^2, a second peak, attributed to the ablatic wave, evolves from the back of the TE wave. At higher power densities, the peaks of the two waves are clearly visible. At the highest power density tested, the AB wave tends to obscure the TE wave. There is also a detectable transverse wave occurring in the ablation regime, where none was detected in the thermoelastic regime. Ablative generation therefore gives rise to a different waveform than thermoelastic generation and subsequently must be considered as a distinct generation mechanism.

Also note in Figure 4 that the resolution of the TE and AB peaks in the echo of the combined waveform is not as pronounced. As the waveform travels through the material, the higher frequencies are attenuated faster than lower frequencies. This attenuation can also be seen in the purely thermoelastic waveforms, below I_{ab}. As a result, the AB wave is much more difficult to discern in thicker samples, or as will be shown later, at significant detection points away from the generation epicenter.

Thermoelastic and Ablatic Amplitude Dependence on Power Density

The data of Fig 4 were analyzed by assuming the waveform $y(t, I)$ at power density I was a superposition of a TE signal $C(I)f(t)$ and an AB signal $D(I)g(t)$. The data were recorded in digital form at times t_i and and discrete intensities I_j. The data set thus consists of m ultrasonic signals $y_{ij} = y(t_i, I_j)$ at n different power densities. The thermoelastic and ablatic waveforms are $f_i = f(t_i)$ and $g_i = g(t_i)$ in similar notation. These are assumed to vary linearly with coefficients $C_j = C(I_j)$ and $D_j = D(I_j)$

$$y_{ij} \approx C_j f_i + D_j g_i. \tag{2}$$

The basis waveforms $f(t)$ and $g(t)$ were arbitrarily assigned unit amplitude at their first maxima. The remaining values of f_i and g_i were determined by a nonlinear fit of the model to the data. The best values of f_i, g_i, C_j and D_j were determined by minimizing the sum

$$S = \sum_{i,j} |y_{ij} - C_j f_i + D_j g_i|^2 \tag{3}$$

with the two unit values of f_i and g_i held constant. For the AS4/PEEK data, there were $n = 38$ intensities and $n = 188$ time-steps between 0.5 and 2.0 μs. For a fit to this data range there were accordingly $mn = 7144$ data and $2(38 + 187) = 450$ free parameters. Figures 6 and 7 show the results of fits to data in this range and to a restricted range between 0.8 and 1.3 mus. Nearly equivalent results were obtained from data in the two ranges.

As stated above, the thermoelastic and ablatic waveforms were arbitrarily assigned unit amplitude at their respective maxima. Otherwise, the forms were completely determined

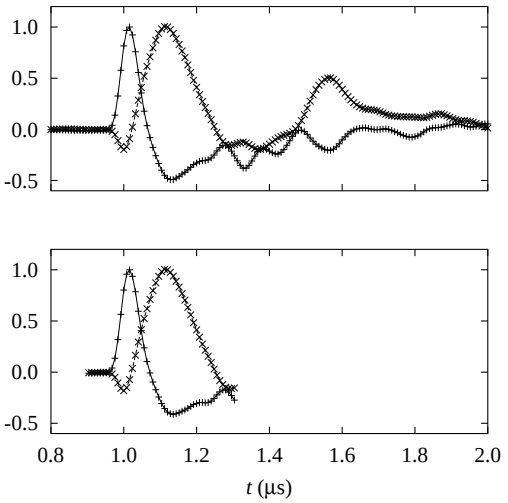

Figure 6: Thermoelastic waveforms $f(t)$ (+) and ablatic waveforms $g(t)$ (×) determined from a fit to the data of Fig 4 as described in the text. The upper plot is for a fit to data for 0.5 μs $\leq t \leq$ 2.0 μs; the lower is for a fit to data in the range 0.8 μs $\leq t \leq$ 1.3 μs. Both plots show that the peak of the ablatic waveform is delated about 0.1 μs with respect to the thermoelastic peak.

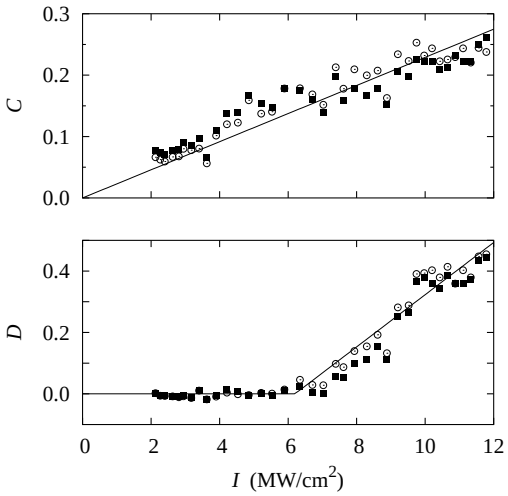

Figure 7: Coefficients C and D of the thermoelastic and ablatic waveforms determined from a fit to the data of Fig 4 as described in the text. The solid symbols were obtained from a fit to data in the range 0.5 μs $\leq t \leq$ 2.0 μs; the open symbols were obtained from a fit to data in the range 0.8 μs $\leq t \leq$ 1.3 μs. The lines are fits to the data as discussed in the main text.

from the data. The TE waveform has a peak at 1.016 μs with a full width at half maxima of 0.053 μs. The AB waveform has a peak at 1.12 μs and a full width at half maximum of 0.13 μs.

Figure 7 shows that the amplitude C of the thermoelastic component varies approximately linearly with the power density over the full range of the experiment. Although there is considerable scatter, fits in the two time ranges are reasonably consistent. The fits also show a distinct threshold for the ablatic wave amplitude D. Equation (1) with a linear dependence ($p = 1$) above the threshold was fit to data in the $0.5 - -2.0$ μs range. The parameters were found to be $a = -0.003 \pm 0.008$, $b = 0.0085 \pm 0.0004$ and $I_{ab} = (62 \pm 2)$. This threshold is in excellent agreement with the value of (59 ± 2)MW/cm^2 determined through photodetection of the ablation plume.

The AB components of the waveforms are displayed separately in Figure 8. These waveforms, obtained by subtracting $\alpha I f(t)$ from the full experimental waveforms, show the evolution of the ablatic with increasing power density. The longitudinal signal and its first echo are clearly resolved, and a transverse

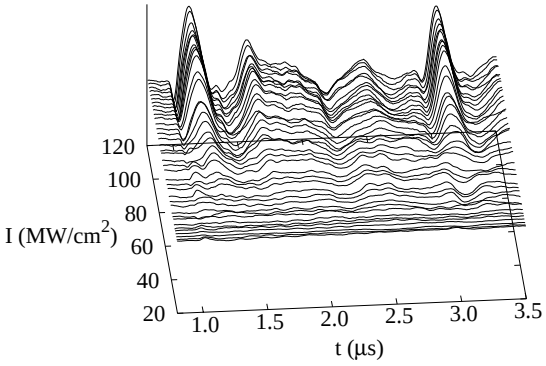

Figure 8: Separated ablatic waveforms plotted as a function of generating laser power density. The waveforms were obtained by subtracting a scaled TE waveform from the full experimental expression. A linear fit applied to the sub-threshold TE coefficients is also shown, demonstrating the proportionality between thermoelastic wave amplitudes and generating laser power density.

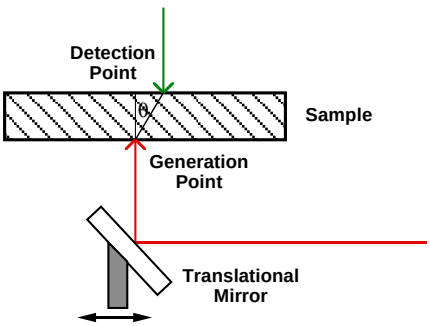

Figure 9: The experimental arrangement for measuring directivity patterns. The angle θ is the directivity angle.

peak is also visible.

The width of the longitudinal wave is much larger ($\approx$ 100 ns) than the width of the TE peak shown in Figure 5 ($\approx$ 35 ns). As evident in Figure 2, the process of ablation lasts over a much longer time than the generating laser pulse. This is consistent with the findings of Kukreja and Hess [16]. It is plausible that the ablative generation process, in comparison with the thermoelastic process, occurs on a longer time scale, and that the AB waveform reaches maximum amplitude at a later time as a consequence.

Directivity Patterns of Thermoelastic and Ablatic Waveforms

The method for establishing the generating mechanism of ablatic waves was put forth by Hutchins *et al.* [6]. Empirical directivity patterns (measuring the ultrasound amplitude as a function of propagation angle) in aluminum were convincingly compared to theoretical patterns, based on the idea that the ablation creates a normal pressure applied to the surface. This has led to the prevailing assertion that the pressures associated with ablation create the AB waves. The shape of the directivity pattern depends on source power density, optical penetration depth [17], and generating spot size. In this case, the diameter of the illuminated area was 5.0 mm. In order to examine the generation mechanism in the composite structure, an experiment for measuring the directivity patterns of ultrasound was carried out.

The experimental arrangement is shown in Figure 9. While the detection point was held fixed, the generating spot was translated from one side of the generating beam axis to the other. The peak-to-peak amplitudes of waveforms at each point were recorded as a function of generation position.

The directivity pattern in the thermoelas-

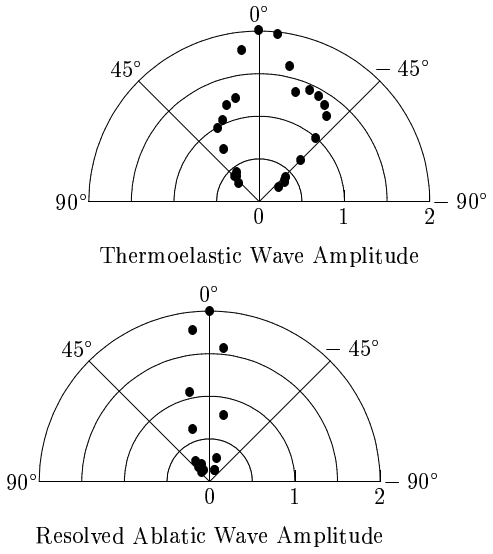

Figure 10: Directivity pattern of thermoelastic and resolved ablatic longitudinal waves in a 16 layer AS-4/PEEK composite panel. The plot shows the dependence of signal amplitude on detection angle.

tic regime is shown in Figure 10. The geometry is rectangular; thus waves travelling at greater angles travel through more material. The waveforms at higher detection angles are attenuated more than waves near the epicenter. Therefore, the directivity pattern becomes more focused. This form is comparable to the theoretical pattern calculated by Dubois *et al.* [18] for an optical penetration depth of 100 μm in isotropic solids. However, given the anisotropic nature of the composite panel, the situations are quite different.

The anisotropy also complicates the directivity pattern. As shown in Scudder *et al.* [19], ultrasonic propagation is heavily dependent on fiber orientation. Waveforms travelling perpendicular to fiber orientation attenuate more than waveforms travelling parallel to fiber orientation [20]. For the case above, this may counteract the focusing produced by the geometry of the test sample.

To directly measure the directivity pattern of the AB component, a simple method which determines the influence of the AB wave on the combined waveform was initiated. The height of the AB peak that projects out of the TE waveform was measured and plotted with angle. Unfortunately, this is more a measure of the resolution of the two waves that results from the attenuation of higher frequencies, than the directivity of the AB waveform.

The resulting directivity pattern is shown in Figure 10. The region where the AB wave can be resolved is quite narrow. For this composite, the wave can only be seen at positions less than 20 degrees (or 1.1 mm) of the epicenter. This does answer the question of why the AB wave seems so elusive. The narrow region for which the AB is resolved from the combined waveform is comparable to the size of the detection laser spot size ($d \approx 0.7$ mm). Waveforms captured with small misalignments in laser beams will not show the waveform.

Ablatic Waveforms in AS-4/PEKK Composite

The ablatic wave experiments were repeated using an 8 layer AS-4/PEKK $[0/90]_{2S}$ composite specimen with a total thickness of 1.5 mm. As with the Gr/PEEK before, a series of ultrasonic waveforms were generated and detected in the panel as the laser power density was increased through the ablation threshold. The resulting waveforms are exhibited in Figure 11. The first longitudinal wave occurred at 430 ns, followed by an echo at 1.3 μs. The first significant ablation was detected at a power density of 113 MW/cm^2. Following this, the ablatic wave peak, superimposed on the back slope of the longitudinal wave, can be seen, especially at higher power densities. The series of

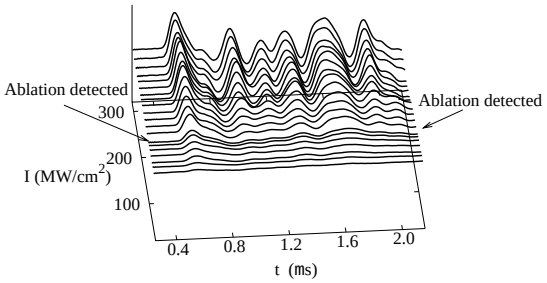

Figure 11: Evolution of the ablatic wave in an 8-layer AS-4/PEKK $[0/90]_{2S}$ composite panel with a total thickness of 1.5 mm. The ablatic wave-peak can be seen to emerge from the back slope of the thermoelastic longitudinal wave.

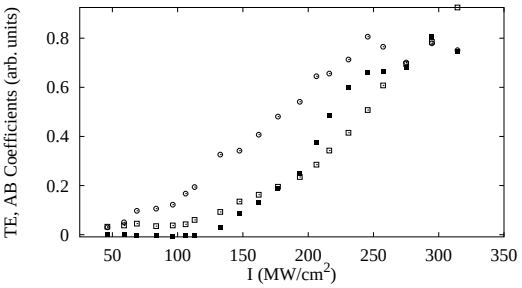

Figure 12: Thermoelastic (open circles) and ablatic (black boxes) coefficients for the AS-4/PEKK composite specimen as a function of laser power density. Also shown are the ablation plume amplitudes (open boxes). The AB coefficients and ablation plume amplitudes exhibit similar thresholds.

peaks occurring between echoes are attributed to a superposition of the TE longitudinal and transverse waves, and the AB longitudinal and transverse waves. Since the sample was comparatively thin, the waves interfere with each other.

Three waveforms with the lowest power densities were averaged to form the TE basis function. The AB basis function was derived by averaging the three highest-intensity waveforms and subtracting off the scaled thermoelastic component. A series of regression fits were then performed on the empirical waveforms using the basis functions.

The coefficients are plotted as a function of power density, along with the signal amplitude of the ablation plume detector, in Figure 12. The TE coefficients show a discernible change in slope near the threshold. The AB coefficients are once again consistent with the ablation plume data, revealing a threshold near 125 MW/cm^2.

There are two significant differences between the ablative effects in this composite and the AS-4/PEEK composite. In contrast to the previous experiment, the TE coefficients have an increase in slope following the detection of ablation. This is possibly a result of some contamination of the TE coefficient by the AB component. Contamination would result if the AB basis function contains a portion of the thermoelastic wave. The second difference is the significantly higher ablation threshold measured in the AS-4/PEKK composite. This is likely a result of greater reflectivity of infrared light by the polymer. Increased reflectivity decreases the absorption of light, thus decreasing the energy deposited in the sample [21]. The laser power density calibration does not account for the reflectivity of the sample. As a result, the ablation threshold, as measured by this method, will be greater. In addition, much higher power densities were needed to detect the two-peaked longitudinal wave. This would also result from the material having a higher reflectivity.

Conclusions

Thermoelastic and ablative generation mechanisms have been investigated in two graphite/polymer composites. Superposition of the TE and AB waveforms, as detected by the CFP-based detection system, was evident for each composite panel. Regression coefficients for each wave type have been calculated and plotted as a function of laser power density, revealing a well-defined ablation threshold. Independent photodetection of light produced by the ablation reaction allowed the correlation of the onset of the ablatic wave and laser ablation. The detection of a transverse wave in the ablation regime, where it had been absent in the thermoelastic regime, provided evidence that ablative generation is a separate and distinct generation mechanism from thermoelastic generation.

Directivity patterns were measured for each wave type in a AS-4/PEEK composite panel. The resolved AB directivity pattern demonstrates the narrow region in which an AB wave can be resolved from the combined waveform. The increased attenuation of the higher frequencies resulted in narrower directivity patterns.

References

[1] R.M. White, *Journal of Applied Physics*, Vol. **14**, no. 12, p. 3559, 1963.

[2] D.A. Hutchins, in *Physical Acoustics,* Vol. **18**, edited by W.P. Mason and R.N. Thurston, (Academic, New York, 1988).

[3] J.C. Miller (Ed.), *Laser Ablation*, (Springer-Verlag: Berlin), 1994.

[4] R. Srinivasan, "Interaction of Laser Radiation with Organic Polymers," p. 107 in reference [3].

[5] P.E. Dyer, S.R. Farrar, and P.H. Key, *Applied Surface Science*, Vol. **54**, p. 255, 1992.

[6] D.A. Hutchins, R.J. Dewhurst, and S.B. Palmer, *Journal of the Acoustical Society of America*, Vol. **70**, no. 5, p. 1362, 1981.

[7] R.J. Dewhurst, D.A. Hutchins, and S.B. Palmer, *Journal of Applied Physics*, Vol. **53**, no. 6, p.4064, 1982.

[8] G.S. Taylor, D.A. Hutchins, C. Edwards, and S.B. Palmer, *Ultrasonics*, Vol. **28**, p. 343, 1990.

[9] P.E. Dyer, and R. Srinivasan, *Applied Physics Letters*, Vol. **48**, no. 10, p. 445, 1986.

[10] J.P. Monchalin, *Applied Physics Letters*, Vol. **47**, p. 14, 1985.

[11] J.P. Monchalin, R. Hèon, R. Bouchard, and C. Padioleau *Applied Physics Letters*, Vol. **55**, p. 1612, 1989.

[12] R.J. Dewhurst and Q. Shan, *Measurement Science and Technology*, Vol. **5**, no. 6, p. 655.

[13] Continuum, 3150 Central Expressway, Santa Clara, CA 95051.

[14] M. Hercher, *Applied Optics*, Vol. **7**, no. 5, p. 951, 1968.

[15] R.G. White, and D.C. Emmony, *Journal of Physics E: Scientific Instruments*, Vol. **18**, p. 658, 1985.

[16] L.M. Kukreja, and P. Hess, *Applied Physics Letters*, Vol. **62**, no. 2, p. 205, 1993.

[17] M. Dubois, M. Choquet, J.P. Monchalin, F. Enguehard, and L. Betrand, *Optical Engineering*, Vol. **32**, no. 9, p. 2255, 1993.

[18] M. Dubois, F. Enguehard, L. Bertrand, M. Choquet, and J.P. Monchalin, *Journal De Physique IV*, Vol. **4**, p. 689, 1994.

[19] L.P. Scudder, D.A. Hutchins, and J.T. Mottram, *Ultrasonics*, Vol. **32**, no. 7, p. 347, 1994.

[20] C. Corbel, F. Guillois, D. Royer, M.A. Fink, and R. De Mol, *IEEE Transactions on Ultrasonics, Ferroelectrics, and Frequency Control*, Vol. **40**, no. 6, p. 710, 1993.

[21] A.D.W. McKie and R.C. Addison, *Ultrasonics*, Vol. **32**, no. 5, p. 333, 1994.